INTERNATIONAL JOURNAL FOR NUMERICAL METHODS IN ENGINEERING
Int. J. Numer. Meth. Engng. 2000; **47**:1343–1361

Multi-scale methods

Wing Kam Liu[*,†,‡], Su Hao[§], Ted Belytschko[¶], Shaofan Li[‖] and Chin Tang Chang[‖]

Department of Mechanical Engineering, Northwestern University, 2145 Sheridan Road, Evanston, IL 60208, U.S.A.

SUMMARY

In this paper four multiple scale methods are proposed. The meshless hierarchical partition of unity is used as a multiple scale basis. The multiple scale analysis with the introduction of a dilation parameter to perform multiresolution analysis is discussed. The multiple field based on a 1-D gradient plasticity theory with material length scale is also proposed to remove the mesh dependency difficulty in softening/localization problems. A non-local (smoothing) particle integration procedure with its multiple scale analysis are then developed. These techniques are described in the context of the reproducing kernel particle method. Results are presented for elastic-plastic one-dimensional problems and 2-D large deformation strain localization problems to illustrate the effectiveness of these methods. Copyright © 2000 John Wiley & Sons, Ltd.

KEY WORDS: multi-scale; meshfree methods; plasticity; localization; mesh dependency; large deformation

1. INTRODUCTION

Meshfree methods, such as smooth particle hydrodynamics (SPH) method and its variations, [1–3], element-free Galerkin method (EFG) [4–6], Reproducing kernel particle method (RKPM), [7–16], multiple scale finite element methods [17], diffuse element method [18], particle in cell methods (PIC) [19], partition of unity [20], marker-and-cell (MAC) method [21], *hp*-cloud method [22–24], finite Point method [25, 26] have been proposed as an alternative to finite element methods. To improve the attributes of this class of meshfree methods, we are incorporating the concepts of reproducing kernel and multiple scale analysis (also referred to as multiresolution analysis in

*Correspondence to: Wing Kam Liu, Department of Mechanical Engineering, Northwestern University, 2145 Sheridan Road, Evanston, IL 60208-3111, U.S.A.
†E-mail: w-liu@nwu.edu
‡Professor of Mechanical and Civil Engineering
§Research Associate
¶Walter P. Murphy, Professor of Computational Mechanics
‖Post-doctoral Fellow

Contract/grant sponsor: ARO
Contract/grant sponsor: NSF
Contract/grant sponsor: AHPCRC

CCC 0029-5981/2000/071343–19$17.50

Received 24 June 1999
Revised 7 July 1999

wavelet theories) into this class of meshfree analysis. Due to their construction, artificial boundaries are generally needed in wavelet and SPH analysis. Both wavelet and SPH methods can be shown to belong to a class of kernel methods where the image/approximation $u^{R_a}(x)$ is given by

$$u^{R_a}(x) = \int_{-\infty}^{+\infty} u(y)\phi_a(x-y)\,\mathrm{d}y \tag{1}$$

In Equation (1), $u(y)$ is the given image data to be reconstructed and $\phi(x)$ can be viewed as a customized low pass filter. In [15, 27–30], Liu and coworkers showed that with the construction of a correction function to SPH (it also applies to scaling functions and wavelets) not only can boundary effect be eliminated, but also the accuracy of discrete solutions can be enhanced throughout the entire domain. To incorporate a correction function, Equation (1) is rewritten as

$$u^{R}(x) = \int_{\Omega} u(y)\bar{\phi}_a(x-y)\,\mathrm{d}y \tag{2}$$

where $\bar{\phi}_a$ is modified window function given by

$$\bar{\phi}_a = C(x;x-y)\phi_a(x-y) \tag{3}$$

where $C(x;x-y)$ is the correction function and Ω is the computational domain. The correction function is of the form

$$C(x;x-y) = b_0(x) + b_1(x)(x-y) + b_2(x)(x-y)^2 + \cdots \tag{4}$$

where $b_i(x)$ are obtained from reproducing conditions. It compensates for the boundary effect. With the corrected scaling functions and wavelets and by varying a dilation parameter 'a', we are able to perform multiresolution analysis on an arbitrary domain using only a set of nodes (or particles). The incorporation of this dilation parameter into the reproducing kernel Equation (2) gives

$$u^{R_a}(x) = \int_{\Omega} u(y)\bar{\phi}_a(x-y)\,\mathrm{d}y = \int_{\Omega} u(y)C_a(x;x-y)\phi_a(x-y)\,\mathrm{d}y \tag{5}$$

One can view $\bar{\phi}_a(x)$ as a window function, so that the integral window transform of $\bar{\phi}_a(x)$ and $u(x)$ is a 'reproduction' of the original $u(x)$ with resolution of $\bar{\phi}_a(x)$. It is equivalent to the convolution, $\bar{\phi}_a * u(x)$. In other words, with the proper design of $\bar{\phi}_a(x)$, $u^{R_a}(x)$ will conserve the resolution and properties of the original solution $u(x)$ up to scale 'a'. For this reason, we prefer to call $\bar{\phi}_a(x)$ and 'a' the scaling function and the scaling (or refinement) parameter, respectively. A smaller 'a' implies a finer scale solution of $u(x)$.

The proposed multiple scale particle method in computational mechanics will consist of the following five tasks.

(i) *Convolution*: The interpolation of the trial function $u(x)$ is considered as the convolution of $u(x)$ with a window function $\phi_a(x)$:

$$u^{R}(x) = \int_{\Omega_y} \phi_a(x-y)u(y)\,\mathrm{d}y \Leftrightarrow \hat{u}^{R}(\omega) = \hat{\phi}_a(\omega)\hat{u}(\omega) \tag{6}$$

(ii) As indicated above, the kernel approximation where $\hat{\phi}_a$ and $\hat{u}$ are Fourier transform of ϕ_a and u and ω is the frequency. In Equation (6), $u(y)$ is a given function to be reconstructed

and $u^R(x)$ is the reconstructed image with the customized filter, $\phi_a(x-y)$. Even though the computations are done in the spatial domain, the interpretation of the solution can be understood in the frequency domain. In this interpretation, the scale is the frequency content of the reconstructed solution.

(ii) *Decomposition of the filters* (*i.e. multiple scale solution*): Due to the fact that a multi-physics problem might contain several scales, it is reasonable to decompose the solution accordingly. By this procedure, each scale can be studied separately:

$$\begin{aligned} u^{R_a}(x) &= \int_{\Omega_y} \phi_{a0}(x-y)u(y)\,\mathrm{d}y + \int_{\Omega_y} \phi_{a1}(x-y)u(y)\,\mathrm{d}y + \int_{\Omega_y} \phi_{a2}(x-y)u(y)\,\mathrm{d}y + \cdots \\ &= u_0^R(x) + u_1^R(x) + u_2^R(x) + \cdots \\ &= \mathrm{Scale}_0 + \mathrm{Scale}_1 + \mathrm{Scale}_2 + \cdots \end{aligned} \tag{7}$$

The construction of these multiple scale filters and selection of scales is described in later sections.

(iii) *Discretize approximation*: For computational purposes, a discretization of the governing equations must be constructed. To interpret Equation (6) discretely, we use (6) gives

$$u^{R_a}(x) = \sum_{I=1}^{\mathrm{NP}} \phi_a(x-x_I)\Delta V_I u_I \tag{8}$$

where ΔV_I is the nodal volume distributed to each particle and u_I is the unknown. The number of particles in the discrete system is denoted by NP. Hence $u^{R_a}(x)$ is discretized to give

$$\begin{aligned} u^{R_a}(x) &= u_0^{R_a}(x) + u_1^{R_a}(x) + u_2^{R_a}(x) + \cdots \\ &= \sum_{I=1}^{\mathrm{NP}} \phi_{a0}(x-x_I)\Delta V_I u_I + \sum_{I=1}^{\mathrm{NP}} \phi_{a1}(x-x_I)\Delta V_I u_I + \cdots \end{aligned} \tag{9}$$

(iv) *Discrete equations*: For a given problem, for each scale a the u_I unknown can be obtained by substituting Equation (8) into the weak form of the equilibrium equations and the additional equations provided by the multi-physics model.

(v) These procedures are described in the subsequent sections.

2. WAVELET APPROACH

The simulation of shear-band formation in an elasto-viscoplastic material by meshless hierarchical basis is shown as an example. To demonstrate the multiresolution properties of meshless methods, a wavelet decomposition is performed in the numerical simulation of shear-band formation. A displacement based meshfree Galerkin formulation is used in the computation. The hierarchical reproducing kernel interpolant for the displacement in terms of the Lagrangian coordinate $\mathbf{X}$ is [31, 32]:

$$u_i(X,t) = \sum_{I=1}^{\mathrm{NP}} \bar{\phi}_{aI}^{[\alpha]}(X)u_{iI}(t) \tag{10}$$

where NP is the total number of particles and α is a multiple index. The reproducing kernel hierarchical interpolant is a partition of unity. It can also be constructed as follows:

$$\bar{\phi}_{a\ell}^{[\alpha]}(X) := \mathbf{P}\left(\frac{X_\ell - X}{a}\right)\mathbf{b}^{(\alpha)}(X)\phi_a(X_\ell - X)\Delta V_\ell \tag{11}$$

In this case, the dimension of the space is $n=2$, $\alpha=(0,0),(1,0),(0,1),(1,1)$; and $X_\ell=(X_{1\ell},X_{2\ell})$, $X=(X_1,X_2)$ are referential coordinates. The vector $\mathbf{b}^{(\alpha)}(X)$ in (11) is determined by the moment equation

$$\begin{pmatrix} m_{00}^h & m_{10}^h & m_{01}^h & m_{11}^h \\ m_{10}^h & m_{20}^h & m_{11}^h & m_{21}^h \\ m_{01}^h & m_{11}^h & m_{02}^h & m_{12}^h \\ m_{11}^h & m_{21}^h & m_{12}^h & m_{22}^h \end{pmatrix} \begin{pmatrix} b_1^{(\alpha)} \\ b_2^{(\alpha)} \\ b_3^{(\alpha)} \\ b_4^{(\alpha)} \end{pmatrix} = \begin{pmatrix} \delta_{\alpha(0,0)} \\ \delta_{\alpha(1,0)} \\ \delta_{\alpha(0,1)} \\ \delta_{\alpha(1,1)} \end{pmatrix} \tag{12}$$

The wavelet multiple scale of this hierarchical partition of unity is given by

$$\begin{aligned} u_i^{\text{total}}(X,t) &= \sum_{I=1}^{\text{NP}} \bar{\phi}_{aI}^{[0,0]}(X)u_{iI}(t) \\ u_i^{\text{high}}(X,t) &= \sum_{I=1}^{\text{NP}} \bar{\phi}_{aI}^{[1,1]}(X)u_{iI}(t) \end{aligned} \tag{13}$$

where u_i^{total} and u_i^{high} are the total scale and high-scale solution, respectively. The low-scale component u_i^{low} is then obtained by subtracting the high-scale component from the total scale. Thus,

$$u_i^{\text{low}}(X,t) = u_i^{\text{total}}(X,t) - u_i^{\text{high}}(X,t) \tag{14}$$

The total and high-scale components of the effective plastic strain, $\bar{\varepsilon}^{\text{total}}$ and $\bar{\varepsilon}^{\text{high}}$, are defined as [35]

$$\begin{aligned} \bar{\varepsilon}^{\text{total}} &= \int_0^t \dot{\bar{\varepsilon}}^{\text{total}}\,\mathrm{d}t \\ \bar{\varepsilon}^{\text{high}} &= \int_0^t \dot{\bar{\varepsilon}}^{\text{high}}\,\mathrm{d}t \end{aligned} \tag{15}$$

The effective plastic strain rate, $\dot{\bar{\varepsilon}}^*$, is defined as

$$\dot{\bar{\varepsilon}}^* = \sqrt{2/3 d_{ij}^{\text{p}*} d_{ij}^{\text{p}*}} \tag{16}$$

where the superscript '$*$' in Equation (16) represents either total scale or high scale. The plastic rate of deformation $d_{ij}^{\text{p}*}$ is given by

$$d_{ij}^{\text{p}*} = d_{ij}^* - d_{ij}^{\text{e}*} \tag{17}$$

The total scale and high-scale components of the rate of deformation, d_{ij}^{total} and d_{ij}^{high}, are evaluated, respectively, by

$$\begin{aligned} d_{ij}^{\text{total}} &= \frac{1}{2}\left(\frac{\partial v_i^{\text{total}}}{\partial x_j} + \frac{\partial v_j^{\text{total}}}{\partial x_i}\right) = \frac{1}{2}\left(\sum_{I=1}^{\text{NP}} \bar{\phi}_{I,j}^{[0,0]}(X,a)v_{iI} + \sum_{I=1}^{\text{NP}} \bar{\phi}_{I,i}^{[0,0]}(X,a)v_{jI}\right) \\ d_{ij}^{\text{high}} &= \frac{1}{2}\left(\frac{\partial v_i^{\text{high}}}{\partial x_j} + \frac{\partial v_j^{\text{high}}}{\partial x_i}\right) = \frac{1}{2}\left(\sum_{I=1}^{\text{NP}} \bar{\phi}_{I,j}^{[1,1]}(X,a)v_{iI} + \sum_{I=1}^{\text{NP}} \bar{\phi}_{I,i}^{[1,1]}(X,a)v_{jI}\right) \end{aligned} \tag{18}$$

where $\partial/\partial x_i$ is the spatial derivative in current configuration, and v_{iI} is the nodal velocity coefficient which is the time derivative of the displacement u_{iI}. The elastic part of the rate of deformation d_{ij}^{e*} is

$$d_{ij}^{e*} = S_{ijkl}^{\text{elas}} \overset{\triangledown}{\sigma}_{kl} \tag{19}$$

where S_{ijkl}^{elas} is the elastic compliance tensor and $\overset{\triangledown}{\sigma}_{kl}$ is the Jaumann rate of Cauchy stress which is computed by

$$\overset{\triangledown}{\boldsymbol{\sigma}} = \dot{\boldsymbol{\sigma}} - \mathbf{w}\boldsymbol{\sigma} + \boldsymbol{\sigma}\mathbf{w}^{\mathrm{T}} \tag{20}$$

The total scale and high-scale components of the spin tensor, w_{ij}^{total} and w_{ij}^{high}, are evaluated, respectively, by

$$\begin{aligned} w_{ij}^{\text{total}} &= \frac{1}{2}\left(\frac{\partial v_i^{\text{total}}}{\partial x_j} - \frac{\partial v_j^{\text{total}}}{\partial x_i}\right) = \frac{1}{2}\left(\sum_{I=1}^{\text{NP}} \bar{\phi}_{I,j}^{[0,0]}(X,a)v_{iI} - \sum_{I=1}^{\text{NP}} \bar{\phi}_{I,i}^{[0,0]}(X,a)v_{jI}\right) \\ w_{ij}^{\text{high}} &= \frac{1}{2}\left(\frac{\partial v_i^{\text{high}}}{\partial x_j} - \frac{\partial v_j^{\text{high}}}{\partial x_i}\right) = \frac{1}{2}\left(\sum_{I=1}^{\text{NP}} \bar{\phi}_{I,j}^{[1,1]}(X,a)v_{iI} - \sum_{I=1}^{\text{NP}} \bar{\phi}_{I,i}^{[1,1]}(X,a)v_{jI}\right) \end{aligned} \tag{21}$$

By subtracting the high-scale component from the total scale component, the low-scale component of the effective plastic strain $\bar{\varepsilon}^{\text{low}}$ can be obtained

$$\bar{\varepsilon}^{\text{low}} = \bar{\varepsilon}^{\text{total}} - \bar{\varepsilon}^{\text{high}} \tag{22}$$

2.1. High-resolution shear-band computation

In this example, a plane strain tension test is simulated for an elasto-viscoplastic material. A velocity of 10 m/s is prescribed at both ends of the tensile bar as shown in Figure 1.

In the numerical simulation, 3321 particles are used. The total solution is shown in Figure 2. By a wavelet transform, it can be decomposed into a low-scale solution and a high-scale solution. Based on this procedure, each scale can be studied separately.

3. MULTIPLE SCALE DECOMPOSITION

From the analysis of Fourier transformation, it is noted that the RKPM kernel function is regarded as a low-pass filter in the reconstruction procedure [28, 29]. The multiple scale RKPM

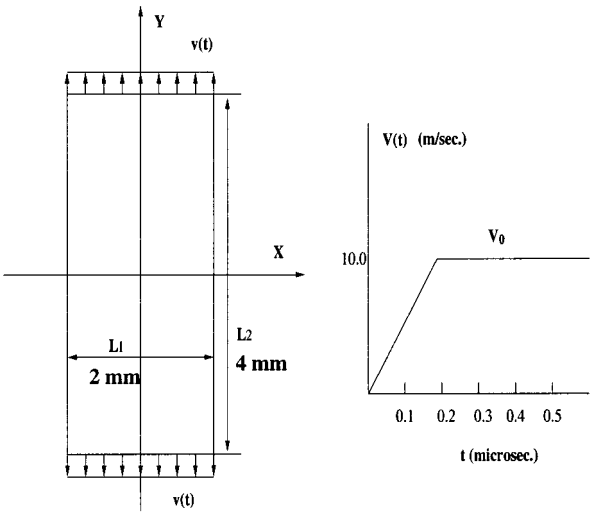

Figure 1. Description of model problem.

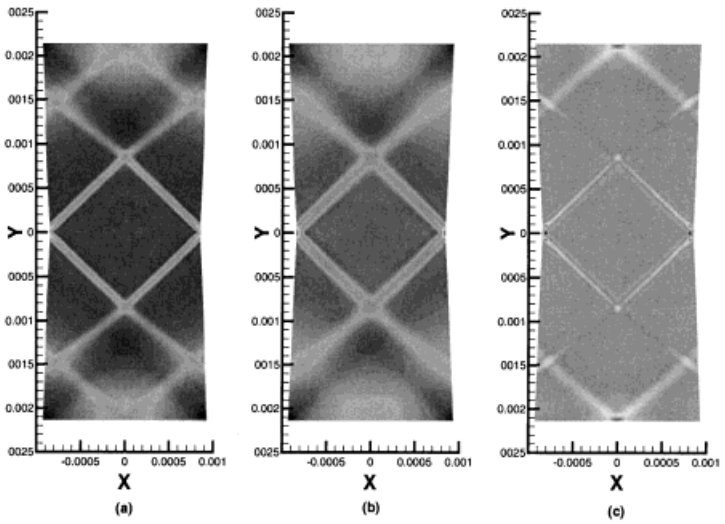

Figure 2. Wavelet's approach for shear-band computation: (a) total scale solution; (b) low-scale solution; and (c) high-scale solution.

is defined by a family of kernel functions. A two-scale decomposition of any response can be written as

$$\begin{aligned} u^{R_a}(x) &= u_0(x) \quad \text{finest scale} \\ &= u_1(x) + w_1(x) \quad \text{two-level decomposition} \end{aligned} \tag{23}$$

where

$$u_1(x) = \int_\Omega C(2a,x,y)\phi(2a,x-y)u(y)\,\mathrm{d}\Omega$$
$$w_1(x) = \int_\Omega \psi(x-y)u(y)\,\mathrm{d}\Omega \tag{24}$$

with

$$\psi(x-y) = C(a,x,y)\phi(a,x-y) - C(2a,x,y)\phi(2a,x-y) \tag{25}$$

where C is the correction function and a is dilation parameter. The discrete counterparts of equation (24) are obtained as

$$u_1(x) = \sum_{J=1}^{\mathrm{NP}} \bar{\phi}_J(x,x_J;2a)u_J \tag{26}$$

$$w_1(x) = \sum_{J=1}^{\mathrm{NP}} [\bar{\phi}_J(x,x_J;a) - \bar{\phi}_J(x,x_J;2a)]u_J \tag{27}$$

in which $\bar{\phi}_J(x)$ is the shape function of RKPM. The two-level decomposition of a function $u^{R_a}(x)$ in discrete form is given as

$$\begin{aligned} u^{R_a}(x) &= \sum_{J=1}^{\mathrm{NP}} \bar{\phi}_J(x;a)u_j \\ &= \sum_{J=1}^{\mathrm{NP}} \bar{\phi}_J(x;2a)u_j + \sum_{J=1}^{\mathrm{NP}} [\bar{\phi}_J(x;a) - \bar{\phi}_J(x;2a)]u_j \\ &= \sum_{J=1}^{\mathrm{NP}} \bar{\phi}_J^{\mathrm{low}}(x;a)u_j + \sum_{J=1}^{\mathrm{NP}} \bar{\phi}_J^{\mathrm{high}}(x;a)u_j \end{aligned} \tag{28}$$

The shape function $\bar{\phi}_J(x)$ is now decomposed into a low-scale (scaling function) component, $\bar{\phi}_J^{\mathrm{low}}(x)$, and a high-scale (wavelet) component, $\bar{\phi}_J^{\mathrm{high}}(x)$. In [8, 14, 33, 34], the application of multiple scale analysis is straightforward. However, for non-linear problems, in particular the problems involved with plastic deformation, the stress and strain cannot be separated as in Equations (26)–(28). Hence, in this paper we redefined the definition of high- and low-scale solutions. The total scale and low-scale components of the effective plastic strain, $\bar{\varepsilon}^{\mathrm{total}}$ and $\bar{\varepsilon}^{\mathrm{low}}$, are defined as [35]:

$$\bar{\varepsilon}^{\mathrm{total}} = \int_0^t \dot{\bar{\varepsilon}}^{\mathrm{total}}\,\mathrm{d}t$$
$$\bar{\varepsilon}^{\mathrm{low}} = \int_0^t \dot{\bar{\varepsilon}}^{\mathrm{low}}\,\mathrm{d}t \tag{29}$$

The definition of the effective plastic strain rate, $\dot{\bar{\varepsilon}}^*$, is the same as in Equation (16), $\dot{\bar{\varepsilon}}^* = \sqrt{2/3 d_{ij}^{\mathrm{p}*} d_{ij}^{\mathrm{p}*}}$, with the superscript '$*$' represents either total scale or low-scale in this section.

Similar to the description in Section 2, the total scale and high-scale components of the rate of deformation, d_{ij}^{total} and d_{ij}^{high} and the spin tensor, w_{ij}^{total} and w_{ij}^{high}, are evaluated accordingly

$$\begin{aligned} d_{ij}^{\text{total}} &= \frac{1}{2}\left(\sum_{I=1}^{\text{NP}} \bar{\phi}_{I,j}(x;a)v_{iI} + \sum_{I=1}^{\text{NP}} \bar{\phi}_{I,i}(x;a)v_{jI}\right) \\ d_{ij}^{\text{low}} &= \frac{1}{2}\left(\sum_{I=1}^{\text{NP}} \bar{\phi}_{I,j}(x;2a)v_{iI} + \sum_{I=1}^{\text{NP}} \bar{\phi}_{I,i}(x;2a)v_{jI}\right) \end{aligned} \tag{30}$$

and

$$\begin{aligned} w_{ij}^{\text{total}} &= \frac{1}{2}\left(\sum_{I=1}^{\text{NP}} \bar{\phi}_{I,j}(x;a)v_{iI} - \sum_{I=1}^{\text{NP}} \bar{\phi}_{I,i}(x;a)v_{jI}\right) \\ w_{ij}^{\text{low}} &= \frac{1}{2}\left(\sum_{I=1}^{\text{NP}} \bar{\phi}_{I,j}(x;2a)v_{iI} - \sum_{I=1}^{\text{NP}} \bar{\phi}_{I,i}(x;2a)v_{jI}\right) \end{aligned} \tag{31}$$

Thus, the high-scale component of the effective plastic strain $\bar{\varepsilon}^{\text{high}}$ is obtained by subtracting the low-scale component from the total scale, as in Equation (22).

3.1. Large deformation fracture and Lueder's bands in a notch-bend specimen

In this section, the deformation process and shear bands in a notch-bend specimen are studied [35]. The setup of a plane-strain notch-bend specimen is shown in Figure 3. According to the classical plastic theory, the slip-line field of the specimen has been constructed and presented in Figure 3. At the upper boundary (Local A), the rigid loading die punches into the specimen and works like a penetration process in metal forming where an idealy lubricated contact surface is assumed. At the crack tip (Local B), a Prandtl's crack tip field is present. These two local fields are connected by the arc-like shear bands. The global slip-line field has the feature of the Green–Henchy solution for a notched bar under pure bending. Thus, the analysed structure represents the basic features of localization phenomenon in the materials.

The geometrical parameters are $a : W : L = 1 : 2 : 8$ with $a = 0.0762$ (m). The deformation processes are considered to be quasi-static. The constitutive law introduced previously has been applied but assuming the visco-plastic effect for the yield stress of the matrix material. That is

$$\frac{\sigma_{\text{y}}}{g(\varepsilon_{\text{eq}})} = \left(\frac{\dot{\varepsilon}_{\text{eq}}}{\dot{\varepsilon}_0}\right)^m \tag{32}$$

where

$$g(\varepsilon_{\text{eq}}) = \begin{cases} \sigma_0 \left(\dfrac{\varepsilon_{\text{eq}}}{\varepsilon_0}\right)^N & \varepsilon_{\text{eq}} \geqslant \varepsilon_0 \\ \sigma_0 & \varepsilon_{\text{eq}} < \varepsilon_0 \end{cases} \tag{33}$$

In the analysis, the material constants are as follows: Young's modulus $E = 210$ GPa, $\sigma_0 = 470$ MPa, Poisson's ratio $v = 0.3$, the strain hardening exponent $N = 0.001$, and the reference strain rate $\dot{\varepsilon}_0 = 0.00218$ with the strain rate exponent $m = 0.001$. The initial void volume fraction $f_0 = 0$ and the volume fraction of second material phase for void nucleation is 0.001.

In the numerical simulation, the specimen is modeled by 5504 RKPM particles. The deformation sequence at different time steps is shown in Figure 4. Large deformation can be observed with the

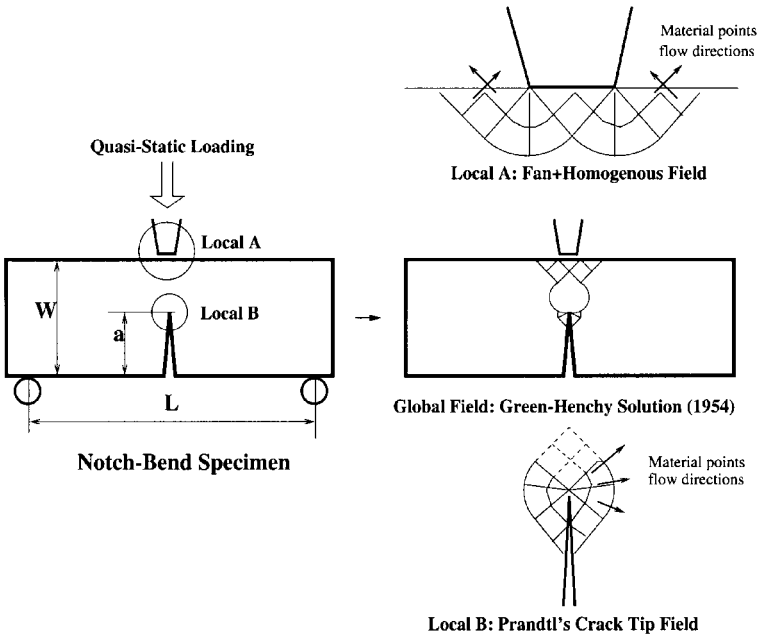

Figure 3. Large deformation fracture and Luders bands in a notch-bend specimen.

loading process. Note that in the computation, only the contact condition between the specimen and the die at the original configuration has been taken into account. To demonstrate the localized deformation around the crack tip and ligament clearly, a close-up of the deformed RKPM particles at the crack tip-ligament area of the specimen is shown in Figure 4. The comparison between particle (meshfree) and mesh-based methods is also presented. As shown in Figure 4, the mesh-based analysis will fail at the final deformation since it leads to a severe mesh distortion. On the contrary, the RKPM computation ran continuously until the right and the left parts of the specimen overlap with each other.

A fine discretization of 22016 particles is also used in the numerical simulation. The comparison between fine and coarse discretizations of the deformation sequence at different time steps is shown in Figure 5. The RKPM multiresolution analysis is performed and compared between fine discretization and coarse discretization. As shown in Figure 6, both the total solution and the high-scale solution capture the location of the Luders band. The fine discretization, however, represents more detailed features of the shear bands which can only be observed in the experimental investigation.

4. MULTIPLE FIELD RKPM

Multiple field RKPM can be viewed as a generalization of the multiple scale method [36]. Thus, fields representing different scales in the problem are incorporated into the formulation, and any overlap between fields is automatically eliminated. Consequently, the consistency of solutions is achieved.

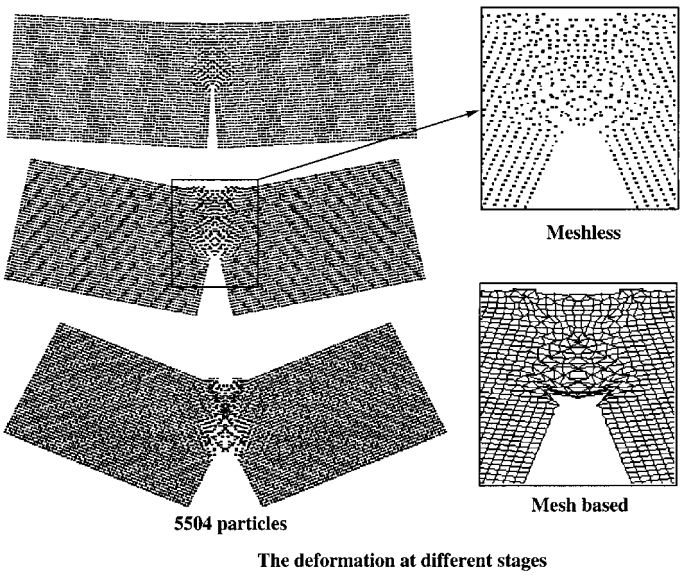

Figure 4. Large deformation fracture of a notch-bend specimen at different time steps.

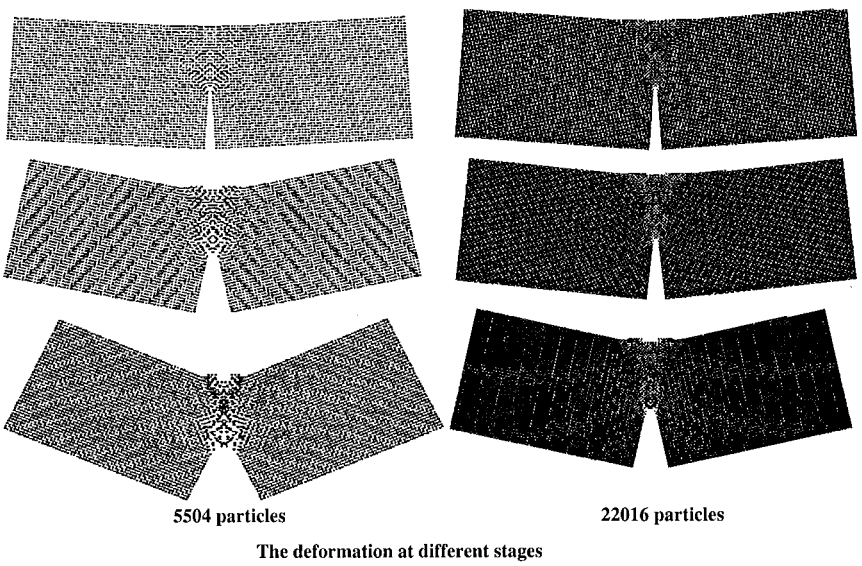

Figure 5. Large deformation fracture of a notch-bend specimen for fine and coarse discretizations.

The basic concept of multiple field RKPM is explained for a two-scale decomposition of $u(x)$:

$$v(x) = v_1(x) + v_2(x) \tag{34}$$

where $v_1(x)$ and $v_2(x)$ are the solutions to different scales or different fields. It will be assumed that $v_1(x)$ and $v_2(x)$ represent the primary and secondary scale/fields of the total solution, $v(x)$.

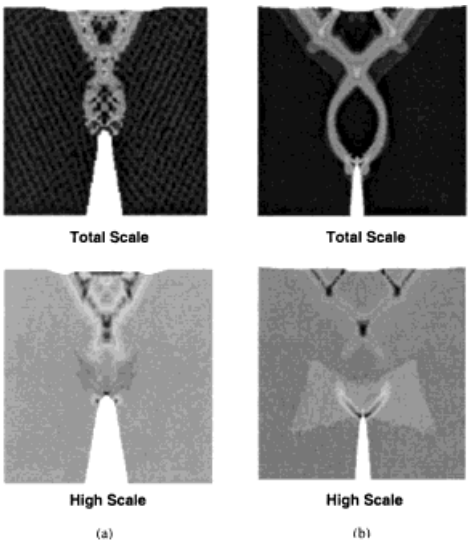

Figure 6. Multiresolution analysis for large deformation fracture of a notch-bend specimen: (a) coarse discretization; and (b) fine discretization.

A sampling projection operator can be defined such that the primary scale/field is reproduced exactly, i.e.

$$v_1(x) = Pv_1(x) \tag{35}$$

Applying the same projection operator, P, to Equation (34) to obtain

$$Pv(x) = Pv_1(x) + Pv_2(x) \tag{36}$$

which is simplified by using Equation (35) to

$$Pv(x) = v_1(x) + Pv_2(x) \tag{37}$$

The primary field, $v_1(x)$, can be solve for from Equation (37), and substituted into Equation (34) to obtain

$$v(x) = Pv(x) - Pv_2(x) + v_2(x) \tag{38}$$

where Pv is the projected solution of v and Pv_2 is the interaction term, and Equation (38) can be interpreted as a general expression for a multiple scale analysis. In particular, if there is no overlapping of scales between $v_1(x)$ and $v_2(x)$, then by the property of the projection operator, the interaction term is zero.

To illustrate the micro–macro material length-scale bridging model, we partition the total displacement into three scales as follows [37]:

$$v^{\text{total}} = v^{\text{hom}} + v^{\text{local}} + v^{\text{bridging}} \tag{39}$$

where $v^{\text{hom}} = Pv(x)$ is the low-scale solution, which is accurate up to the continuum scale using a micro-mechanical material model without a length scale. This solution can be approximated by the usual FEM or a meshfree method. $v^{\text{local}} = v_2(x)$ is the material length-scale solution, which is a function of the length-scale material model and the low-scale solution. $v^{\text{bridging}} = -Pv_2(x)$ is the bridging scale solution. It is noted that the length scale can be of order of 1 μm micron or less. The local, homogeneous, bridging and total strain rates can similarly be defined by differentiating the above equation:

$$\dot{\varepsilon}^{\text{total}} = \dot{\varepsilon}^{\text{hom}} + \dot{\varepsilon}^{\text{local}} + \dot{\varepsilon}^{\text{bridging}} \tag{40}$$

For demonstration purpose, we have developed a v^{local} solution which is based on a 1-D gradient plasticity theory with material length scale. The governing equation can be simplified as

$$F_0 + F_1 \frac{\mathrm{d}v^{\text{local}}}{\mathrm{d}x} + l\frac{\mathrm{d}^2 v^{\text{local}}}{\mathrm{d}x^2} = 0 \tag{41}$$

with

$$v^{\text{local}}|_{x=0} = 0, \quad \left.\frac{\mathrm{d}v^{\text{local}}}{\mathrm{d}x}\right|_{x=\pm w/2} = 0, \quad \left.\frac{\mathrm{d}^2 v^{\text{local}}}{\mathrm{d}x^2}\right|_{x=0} = 0 \tag{42}$$

and

$$\begin{aligned} F_0 &= 2\left[f(\bar{\varepsilon}^{\text{total}})f'(\bar{\varepsilon}^{\text{total}}) - f(\bar{\varepsilon}^{\text{hom}})f'(\bar{\varepsilon}^{\text{hom}})\left(\frac{f^2(\bar{\varepsilon}^{\text{total}}) + l\bar{\eta}^{\text{total}}}{f^2(\bar{\varepsilon}^{\text{hom}}) + l\bar{\eta}^{\text{hom}}}\right)^{1/2}\right]\dot{\varepsilon}_{11}^{\text{hom}} \\ F_1 &= 2f(\bar{\varepsilon}^{\text{total}})f'(\bar{\varepsilon}^{\text{total}}) \end{aligned} \tag{43}$$

The decomposed velocity fields are defined as:

$$\begin{aligned} \mathbf{v}^{\text{total}} &= \mathbf{v}^{\text{hom}} + \mathbf{v}^{\text{local}} \\ \dot{\boldsymbol{\varepsilon}}^{\text{total}} &= \dot{\boldsymbol{\varepsilon}}^{\text{hom}} + \dot{\boldsymbol{\varepsilon}}^{\text{local}} \\ \dot{\boldsymbol{\eta}}^{\text{total}} &= \dot{\boldsymbol{\eta}}^{\text{hom}} + \dot{\boldsymbol{\eta}}^{\text{local}} \end{aligned} \tag{44}$$

where

$$\dot{\boldsymbol{\eta}}^{\text{local}} = \tfrac{1}{2}(\mathbf{gn} + \mathbf{ng}) \tag{45}$$

with

$$\mathbf{g} = \partial \mathbf{v}^{\text{local}}/\partial x_n, \ \mathbf{n} \text{ the unit normal to the surface (see Figure 7)} \tag{46}$$

In [37], the $\mathbf{v}^{\text{local}}$ solution is obtained numerically and analytically.

4.1. A rod under tension

In conjunction with the recent development of strain gradient theory, the multiple field RKPM can be applied for simulating strain localization problem. For the specimen illustrated in Figure 3, the corresponding multiple fields are shown in Figure 7 where the high-scale solution is computed by embedding the 1-D solution in **n** direction.

The problem statement of the 1-D case in Section 3.4 is given in Figure 8. In the computations, the following material parameters are used in both tests: $E = 2000$, $E_t = -1$, $\sigma_Y = 1$, $e_Y = 1/2000$, and $l = 5.0\text{e}^{-4}$ mm.

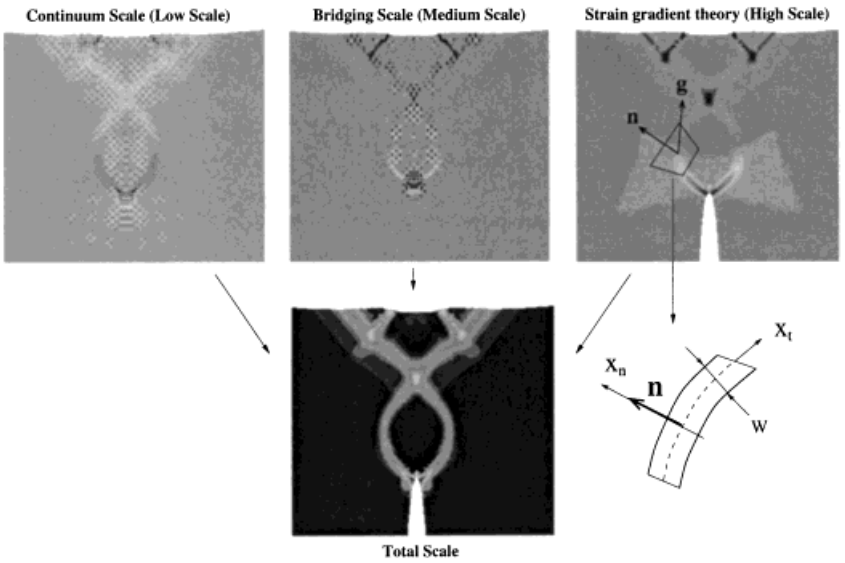

Figure 7. Multiple scale decomposition of the localization field in a notched bending bar.

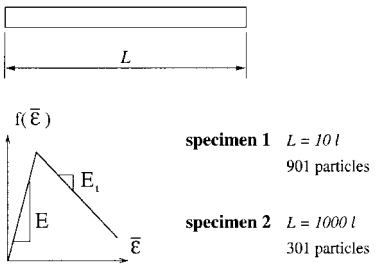

Figure 8. Localization in a rod.

The numerical interpolated localization solution for this 1-D case is given as [37]

$$v^{\text{local}} = \frac{F_0}{F_1 B}\left[\frac{B-1}{B[1-B^2l^2/f^2(\bar{\varepsilon}^{\text{total}})]}\left(\exp^{-Bx} - \frac{B^2l^2}{f^2(\bar{\varepsilon}^{\text{total}})}\exp^{f(\bar{\varepsilon}^{\text{total}})/l}\right) - 1 - Bx\right]$$

with

$$B = \frac{f(\bar{\varepsilon}^{\text{total}})}{l} + \frac{l}{w} \quad \text{and} \quad \dot{\varepsilon}^{\text{local}} = \frac{\mathrm{d}v^{\text{local}}}{\mathrm{d}x_1} \tag{47}$$

The numerical interpolated width of the localization zone w is given as

$$w = \frac{1}{\beta}\tan^{-1}\frac{\alpha}{\beta} \tag{48}$$

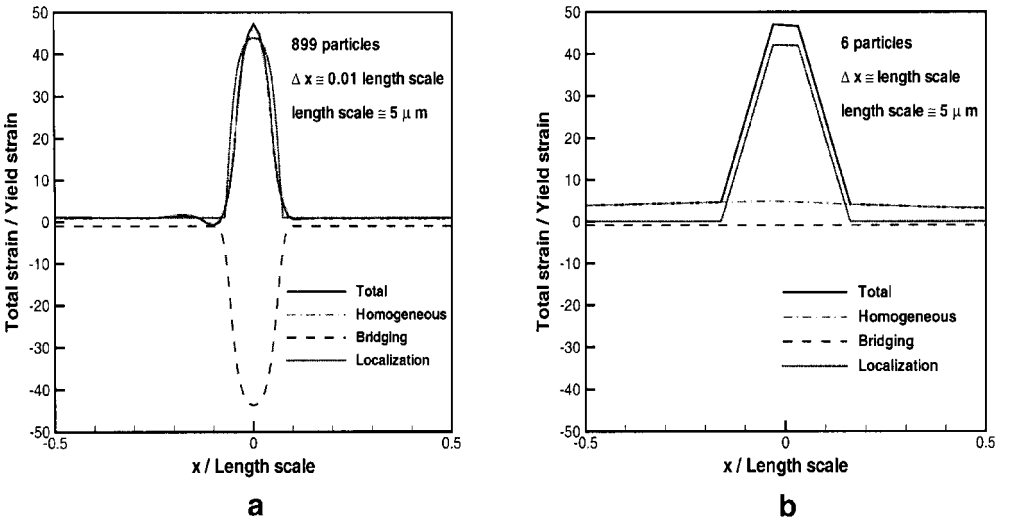

Figure 9. A rod under tension: multi-scale analysis of gradient plasticity: (a) fine discretization; and (b) coarse discretization.

where

$$\alpha = 2f(\bar{\varepsilon})f'(\bar{\varepsilon})$$
$$\beta = \alpha^2 + 2\frac{f(\bar{\varepsilon})}{\sigma_Y}(E_t - E) \tag{49}$$

Its solutions at the localized region (over 8 material length scale) are depicted in Figure 9 for a bar pulled at both ends. The bridging solutions u^{bridging} and $\varepsilon^{\text{bridging}}$, are then constructed following the multiple-field solution procedure given in Liu *et al.* [36]. It is plotted in Figure 6 along with the total strain solutions. Figure 9(a) is obtained using a fine discretization (901 particles for 8 material length scale). Figure 9(b) is obtained using a coarse discretization with Δx (the distance between two particles) much greater than the material length scale. Obviously, $\varepsilon^{\text{bridging}}$ is significant in the fine discretization model and it is almost equal to zero in the coarse discretization model (see Figure 9(b)). The total strain distributions, however, are the same. Hence, we believe that with such a micro-to-macro material length scale bridging model, the micro solution can be obtained with a very coarse discretization (i.e. ($x \gg$ material length scale). Comparing the fine and coarse discretization solutions (Figures 9(a) and 9(b)), it can be concluded that this multi-scale–multi-physic solution is mesh independent.

Even though the micro-scale solution gives a high-amplitude plastic strain in a narrow band, as shown in Figure 9, the width is of the order of the material length-scale. This width is too small to be computed from a macro (continuum) solution, as illustrated in Figure 10(a). Consequently, the difficulty associated with numerically capturing strain localizations and fracture in solids has posed a serious challenge in the computational mechanics community. The proposed method is able to embed higher resolutions (scales) within the framework of wavelet packets and multi-physics solution enrichment without any additional nodes. From the above illustration, we have demonstrated that the bridging scale solution indeed bridges the material length-scale solution to

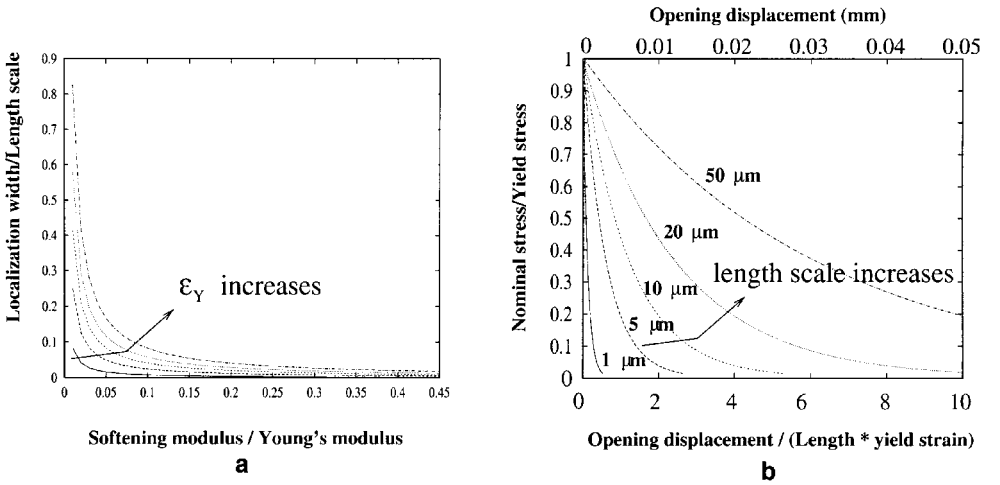

Figure 10. A rod under tension: material length scale: (a) micro-localization-induced force versus strain curve; and (b) nominal stress versus opening displacement.

the continuum meso-scale solution. As can be seen in Figure 10(b), fracture and fragmentation can be modelled by this 'micro-localization-induced force versus strain curve'. It can be seen that the nominal stress (or the separation force) and the opening displacement are strong functions of the material length-scale (see Figure 10). In this manner, a micro-scale discretized crack initiation, micro-scale crack growth (order of the material length-scale) and ultimate growth to fracture and fragmentation sequence can be predicted.

5. NON-LOCAL PARTICLE APPROACH

In this section, a non-local (smoothing) particle integration procedure is proposed. Using Taylor series expansion about node x_A to compensate underintegration

$$\mathscr{F}(\mathbf{x}) = \mathscr{F}(\mathbf{x}_A) + \mathscr{F}_{,x}(\mathbf{x}_A)(\mathbf{x} - \mathbf{x}_A) \tag{50}$$

where variable $\mathscr{F}(x)$ can be $u(x)$, $\delta\boldsymbol{\varepsilon}(x)$ or $\boldsymbol{\sigma}(x)$. Here, the set of points x_A may be any points about which we choose to take our Taylor expansion. In an effort to work toward a nodally based numerical scheme, we will take x_A as nodal points. In large deformation problems, however, this nodally based numerical scheme may results in unstable deformation pattern. Thus, a nonlocal (smoothing) approximation is introduced in this section [38]. In the nonlocal approximation, a variable $\mathscr{F}(x)$ and its derivatives at $\mathbf{x}_A$ are replaced by

$$\begin{array}{ccc} \mathscr{F}(\mathbf{x}) = & \mathscr{F}(\mathbf{x}_A) + & \mathscr{F}_{,x}(\mathbf{x}_A)(\mathbf{x} - \mathbf{x}_A) \\ & \Uparrow & \Uparrow \\ & \langle \mathscr{F}(\mathbf{x}_A) \rangle & \langle \mathscr{F}_{,x}(\mathbf{x}_A) \rangle \end{array} \tag{51}$$

Define the non-local RKPM smoothing operators as (for $\mathbf{x}_A \in \Omega_J$)

$$\begin{aligned}\langle \mathscr{F}(\mathbf{x}_A)\rangle &= \int_{\Omega_A} \Phi(x_A - \xi)\mathscr{F}(\xi)\,\mathrm{d}\xi = \sum_{K=1}^{\mathrm{NPS}_A} N_K(\mathbf{x}_A)\mathscr{F}(\mathbf{x}_K)\\ \langle \mathscr{F}_{,x}(\mathbf{x}_A)\rangle &= \int_{\Omega_A} \Phi_{\,x}(x_A - \xi)\mathscr{F}(\xi)\,\mathrm{d}\xi = \sum_{K=1}^{\mathrm{NPS}_A} N_{K,x}(\mathbf{x}_A)\mathscr{F}(\mathbf{x}_K)\end{aligned} \tag{52}$$

where the number of particles in the smoothing region for a subdomain Ω_A is denoted by NPS_A.

Partition the domain of node J into M (for example, in the algorithm shown below: $M = 3$) subdomains. Hence, the J_{th} nodal internal force

$$\mathbf{F}_J = \int_\Omega \mathbf{B}_J^{\mathrm{T}}\boldsymbol{\sigma}\,\mathrm{d}\Omega \simeq \int_{S_{J-1}} \bar{\mathbf{B}}_{J(J-1)}^{\mathrm{T}}\boldsymbol{\sigma}\,\mathrm{d}S_{J-1} + \int_{S_J} \bar{\mathbf{B}}_{J(J)}^{\mathrm{T}}\boldsymbol{\sigma}\,\mathrm{d}S_J + \int_{S_{J+1}} \bar{\mathbf{B}}_{J(J+1)}^{\mathrm{T}}\boldsymbol{\sigma}\,\mathrm{d}S_{J+1} \tag{53}$$

Substitute Equations (51) and (52) into the above relation, one gets

$$\begin{aligned}\mathbf{F}_J^{\mathrm{int}} &= \sum_{A\in\Omega_J}\Big[\int_{S_A}\langle \mathbf{B}_J^{\mathrm{T}}(\mathbf{x}_A)\rangle\langle\boldsymbol{\sigma}(\mathbf{x}_A)\rangle\,\mathrm{d}S_A + \int_{S_A}\langle \mathbf{B}_J^{\mathrm{T}}(\mathbf{x}_A)\rangle\langle\boldsymbol{\sigma}_{,x}(\mathbf{x}_A)\rangle(\mathbf{x}-\mathbf{x}_A)\,\mathrm{d}S_A\\ &\quad + \int_{S_A}\langle \mathbf{B}_{J,x}^{\mathrm{T}}(\mathbf{x}_A)\rangle\langle\boldsymbol{\sigma}(\mathbf{x}_A)\rangle(\mathbf{x}-\mathbf{x}_A)\,\mathrm{d}S_A + \int_{S_A}\langle \mathbf{B}_{J,x}^{\mathrm{T}}(\mathbf{x}_A)\rangle\langle\boldsymbol{\sigma}_{,x}(\mathbf{x}_A)\rangle(\mathbf{x}-\mathbf{x}_A)^2\,\mathrm{d}S_A\Big]\\ &= \langle F_J\rangle_0 + \langle F_J\rangle_{\mathrm{stab}}\end{aligned} \tag{54}$$

with

$$\begin{aligned}\langle F_J\rangle_0 &= \sum_{A\in\Omega_J}\langle \mathbf{B}_J^{\mathrm{T}}(\mathbf{x}_A)\rangle\langle\boldsymbol{\sigma}(\mathbf{x}_A)\rangle M_A^0\\ \langle F_J\rangle_{\mathrm{stab}} &= \sum_{A\in\Omega_J}[\langle \mathbf{B}_J^{\mathrm{T}}(\mathbf{x}_A)\rangle\langle\boldsymbol{\sigma}_{,x}(\mathbf{x}_A)\rangle + \langle \mathbf{B}_{J,x}^{\mathrm{T}}(\mathbf{x}_A)\rangle\langle\boldsymbol{\sigma}(\mathbf{x}_A)\rangle]M_A^1\\ &\quad + \sum_{A\in\Omega_J}\langle \mathbf{B}_{J,x}^{\mathrm{T}}(\mathbf{x}_A)\rangle\langle\boldsymbol{\sigma}_{,x}(\mathbf{x}_A)\rangle M_A^2\end{aligned} \tag{55}$$

where the moments from computational geometry are defined by

$$M_A^0 = \int_{S_A}\mathrm{d}S_A, \quad M_A^1 = \int_{S_A}(\mathbf{x}-\mathbf{x}_A)\,\mathrm{d}S_A, \quad M_A^2 = \int_{S_A}(\mathbf{x}-\mathbf{x}_A)^2\,\mathrm{d}S_A \tag{56}$$

By using Equations (51) and (52), the reproducing kernel interpolants with the non-local (smoothing) approximation u^{S_A} and $\boldsymbol{\varepsilon}^{S_A}$ are

$$\begin{aligned}u^{S_A}(x) &= \sum_{J=1}^{\mathrm{NP}} N_J(x)\sum_{K=1}^{\mathrm{NPS}_A}[N_K(x_J) + B_K(x_J)M_K^1]u(x_K)\\ \boldsymbol{\varepsilon}^{S_A}(x) &= \sum_{J=1}^{\mathrm{NP}} B_J(x)\sum_{K=1}^{\mathrm{NPS}_A}[N_K(x_J) + B_K(x_J)M_K^1]u(x_K)\end{aligned} \tag{57}$$

The multiple scale analysis of non-local smoothing fields can be expressed as

$$\mathscr{F}^{\mathrm{high}}(x) = \mathscr{F}^{R_a}(x) - \mathscr{F}^{S_A}(x) \tag{58}$$

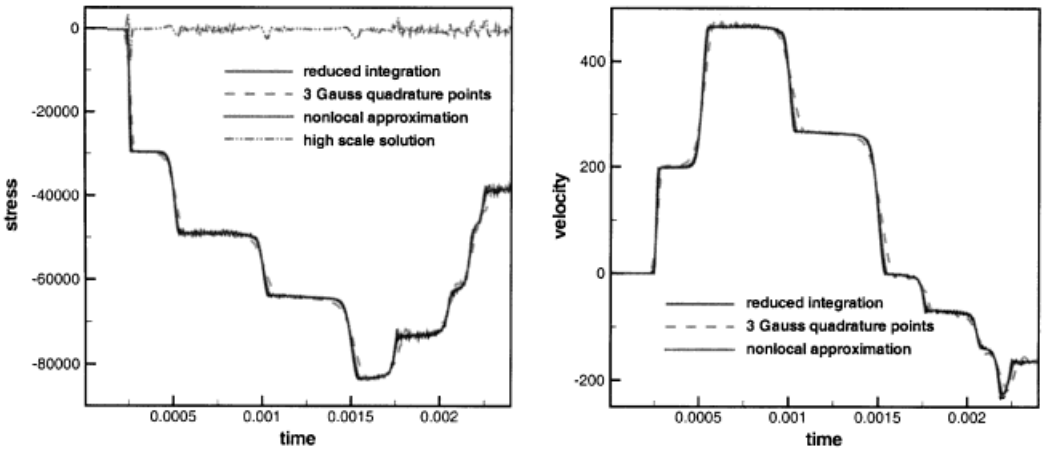

Figure 11. Stress and velocity at the center of elastic–plastic bar under compression.

where variable $\mathscr{F}$ can be $u(x), \delta\boldsymbol{\varepsilon}(x)$ or $\boldsymbol{\sigma}(x)$ and the superscript S_A and R_a are denoted as the reproducing kernel interpolants with and without the non-local (smoothing) approximation, respectively.

5.1. 1-D elastic/plastic wave

Results are presented for a one-dimensional bar subjected to an impact load. An elastic–plastic material model was used with the following properties: Young's modulus $E = 3 \times 10^7$ psi, $\rho_0 = 7.24 \times 10^{-4}$, the cross section area $A = 1.0$ in^2, $E_{\mathrm{p}} = 7.5 \times 10^6$ psi and $\sigma_{\mathrm{y}} = 30\,000$ psi. Time integration was performed using a Newmark-β predictor–corrector algorithm ($\beta = 0, \gamma = 0.505$)

Two other integration methods are used for RKPM for comparison, 3-point Gauss quadrature scheme and the reduced integration scheme. Figure 11 show the stress and velocity at the centre of the bar for a compressive step load of $\sigma_0 = 50\,000$ psi. As can be seen from these figures, the tensile instability associated with SPH [39] has been eliminated through the use of the correction function. The solution is slightly more accurate with reduced integration. However, when single-point Gaussian integration was used, no solution was achieved. The high-scale solution of the stress computed by Equation (58) is also shown in Figure 11.

5.2. Impact problem

As an example, the impact/penetration process of a disk hitting a steel target has been simulated [38]. The disk is assumed rigid with a given initial velocity of 3000 M/s. The target steel is modelled by the Johnson–Cook constitutive law (visco-plasticity) with damage where the failure of a material point occurs when the damage reaches its critical value and the stress level approaches to zero.

Figure 12 depicts the time history of the damage evolution of the target. A complete description of this problem is given in [38].

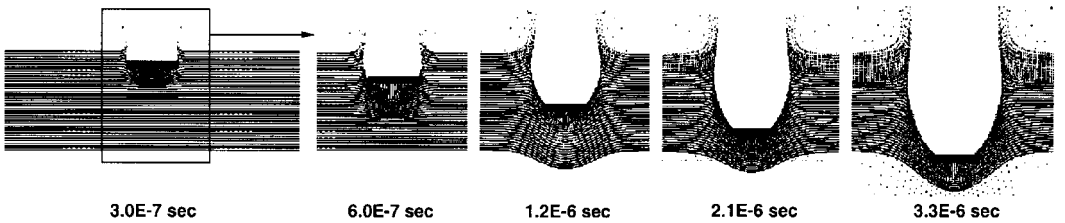

Figure 12. Simulation of penetration process using truly multiple scale meshfree method.

6. CONCLUSION

In this paper, several multiple scale techniques have been demonstrated and used successfully in meshfree computations in solving large deformation problems of inelastic solids, such as shear band formation and impact/fragmentation. This class of methods has a build-in capacity to decompose the resolved numerical solutions into different scales. The associated physical phenomena can be interpreted according to the different scales of the numerical solutions. In addition, the proposed multiple scale method, especially the one introduced in Section 4, may significantly reduce the mesh dependency that usually occurs in numerical simulation of strain localization problems.

All these approaches are basically a spectral decomposition of the numerical solutions, which is different from the usual notions of *h*-refinement or *p*-refinement in finite element method, we believe that a new class of spectral refinement/decomposition algorithms can be constructed by using this class of multi-scale meshfree particle methods.

ACKNOWLEDGEMENTS

The support of this research by Army Research Office(ARO) and National Science Foundation (NSF) to Northwestern University is gratefully acknowledged.

Sponsored in part by the Army High Performance Computing Research Center (AHPCRC) under the auspices of the Department of the Army Research Laboratory. The content does not necessarily reflect the position or the policy of the government, and no official endorsement should be inferred.

REFERENCES

1. Gingold RA, Monaghan JJ. Smoothed particle hydrodynamics: theory and application to non-spherical stars. *Monthly Notices of the Royal Astronomical Society* 1977; **181**:375–389.
2. Gingold RA, Monaghan JJ. Kernel estimates as a basis for general particle methods in hydrodynamics. *Journal of Computational Physics* 1982; **46**:429–453.
3. Lucy L. A numerical approach to testing the fission hypothesis. *Astronomical Journal* 1977; **82**:1013–1024.
4. Belytschko T, Krongauz Y, Organ D, Fleming M, Krysl P. Meshless methods: an overview and recent developments. *Computer Methods in Applied Mechanics and Engineering* 1996; **139**:3–47.
5. Belytschko T, Lu YY, Gu L. Element free Galerkin methods. *International Journal for Numerical Methods in Engineering* 1994; **37**:229–256.
6. Belytschko T, Lu YY, Gu L. A new implementation of the element free Galerkin method. *Computer Methods in Applied Mechanics and Engineering* 1994; **113**:397–414.
7. Hao S, Liu WK, Chang CT. Computer implementation of damage models by finite element and meshfree methods. *Computer Methods in Applied Mechanics and Engineering* 1998; accepted for publication, to appear (In press).
8. Jun S, Liu WK, Belytschko T. Explicit reproducing kernel particle methods for large deformation problems. *International Journal for Numerical Methods in Engineering* 1998; **41**:137–166.
9. Liu WK. An introduction to wavelet reproducing kernel particle methods. *USACM Bulletin* 1995; **8**(1):3–16.

10. Liu WK, Chang CT, Chen Y, Uras RA. Multiresolution reproducing kernel particle methods in acoustic problems. *Acoustics, Vibrations, and Rotating Machines*, DE-vol.84-2, Part B. ASME: New York, 1995; 881–900.
11. Liu WK, Chen Y, Chang CT, Belytschko T. Advances in multiple scale kernel particle methods. *A Special Feature Article for the 10th Anniversary Volume of Computational Mechanics* 1996; **18**(2):73–111.
12. Liu WK, Chen Y, Jun S, Chen JS, Belytschko T, Pan C, Uras RA, Chang CT. Overview and applications of the reproducing kernel particle methods. *Archives of Computational Methods in Engineering*; *State of the Art Reviews* 1996; **3**:3–80.
13. Liu WK, Chen Y, Uras RA, Chang CT. Generalized multiple scale reproducing kernel particle methods. *Computer Methods in Applied Mechanics and Engineering* 1996; **139**:91–158.
14. Liu WK, Jun S. Multiple scale reproducing kernel particle methods for large deformation problems. *International Journal for Numerical Methods in Engineering* 1998; **41**:1339–1362.
15. Liu WK, Jun S, Zhang YF. Reproducing kernel particle methods. *International Journal for Numerical Methods in Fluids* 1995; **20**:1081–1106.
16. Liu WK, Li S, Belytschko T. Moving least square kernel Galerkin method (I) methodology and convergence. *Computer Methods in Applied Mechanics and Engineering* 1997; **143**:113–154.
17. Liu WK, Zhang Y, Ramirez MR. Multiple scale finite element methods. *International Journal for Numerical Methods in Engineering* 1991; **32**:969–990.
18. Nayroles B, Touzot G, Villon P. Diffuse approximation and diffuse elements. *Computational Mechanics* 1992; **10**: 307–318.
19. Sulsky D, Chen Z, Schreyer HL. A particle method for history-dependent materials. *Computer Methods in Applied Mechanics and Engineering* 1994; **118**:179–196.
20. Babuska I, Melenk JM. The partition of unity finite element method. *University of Maryland Technical Note BN-1185*, 1995.
21. Harlow FH, Welch JE. Numerical study of large-amplitude free-surface motion. *Physics of Fluids* 1966; **9**:842–851.
22. Duarte CA, Oden JT. Hp clouds—a meshless method to solve boundary-value problems. *TICAM Report 95-05*, 1995.
23. Duarte CA, Oden JT. An hp adaptive method using clouds. *Computer Methods in Applied Mechanics and Engineering* 1996.
24. Duarte CA, Oden JT. Hp clouds—an hp meshless method. *Numerical Methods for Partial Differential Equations* 1996.
25. Oñate E, Idelsohn S, Fischer T, Zienkiewicz OC. A finite point methods for analysis of fluid flow problems. *Presented in 9th International Conference on Finite Elements in Fluids*, Venezia, Italy, 1995; 15–21.
26. Oñate E, Idelsohn S, Zienkiewicz OC. Finite point methods in computational mechanics. *International Center for Numerical Methods in Engineering* 1995.
27. Liu WK, Adee J, Jun S. Reproducing kernel and wavelet particle methods for elastic and plastic problems. In *Advanced Computational Methods for Material Modeling*, Benson DJ, Asaro RA (eds), AMD 180 and PVP 268. ASME: New York, 1993; 175–190.
28. Liu WK, Chen Y. Wavelet and multiple scale reproducing kernel methods. *International Journal for Numerical Methods in Fluids* 1995; **21**:901–931.
29. Liu WK, Jun S, Li S, Adee J, Belytschko T. Reproducing kernel particle methods for structural dynamics. *International Journal for Numerical Methods in Engineering* 1995; **38**:1655–1679.
30. Liu WK, Oberste-Brandenburg C. Reproducing kernel and wavelet particle methods. In *Aerospace Structures: Nonlinear Dynamics and System Response*, Cusumano JP, Pierre C, Wu ST (eds), AD33. ASME: New York, 1993; 39–56.
31. Li S, Liu WK. Reproducing kernel hierarchical partition of unity, part I: formulation and theory. *International Journal for Numerical Methods in Engineering* 1999; **45**:251–288.
32. Li S, Liu WK. Reproducing kernel hierarchical partition of unity, part II: applications. *International Journal for Numerical Methods in Engineering* 1999; **45**:289–317.
33. Gunther FC, Liu WK. Implementation of boundary conditions for meshless methods. *Computer Methods in Applied Mechanics and Engineering* 1998; **163**:205–230.
34. Liu WK, Jun S, Sihling DT, Chen Y, Hao W. Multiresolution reproducing kernel particle method for computational fluid dynamics. *International Journal for Numerical Methods in Fluids* 1997; **24**:1391–1415.
35. Hao S, Liu WK, Belytschko T. Multiple-scale analysis of localization and fracture. *Technical Report*, Department of Mechanical Engineering, Northwestern University, 1999.
36. Liu WK, Uras RA, Chen Y. Enrichment of the finite element method with the reproducing kernel particle method. *Journal of Applied Mechanics*, ASME 1998; **64**:861–870.
37. Hao S, Liu WK. Localization induced band and cohesive model. *Journal of Applied Mechanics* 1999; submitted.
38. Hao S, Liu WK, Belytschko T. Nonlocal particle method. *Technical Report*, Department of Mechanical Engineering, Northwestern University, 1999.
39. Attaway SW, Heinstein NW, Mello FJ, Swegle JW. Coupling of smooth particle hydrodynamics with pronto. 1993.

